MNRAS 000, 1–?? (0000) Preprint 29 September 2022 Compiled using MNRAS LATEX style file v3.0

Orientation effects on cool gas absorption from gravitational-arc tomography of a $z = 0.77$ disc galaxy

A. Fernandez-Figueroa,[1] S. Lopez,[1⋆] N. Tejos,[2] T. A. M. Berg,[1,3] C. Ledoux,[3] P. Noterdaeme,[4,5] A. Afruni,[1] L. F. Barrientos,[6] J. Gonzalez-Lopez,[7,8] M. Hamel,[1] E. J. Johnston,[8] A. Katsianis,[9] K. Sharon[10] and M. Solimano[8]

[1] *Departamento de Astronomía, Universidad de Chile, Casilla 36-D, Santiago, Chile*
[2] *Instituto de Física, Pontificia Universidad Católica de Valparaíso, Casilla 4059, Valparaíso, Chile*
[3] *European Southern Observatory, Alonso de Córdova 3107, Vitacura, Casilla 19001, Santiago, Chile*
[4] *Franco-Chilean Laboratory for Astronomy, IRL 3386, CNRS and Universidad de Chile, Santiago, Chile*
[5] *Institut d'Astrophysique de Paris, CNRS-SU, UMR 7095, 98bis bd Arago, 75014 Paris, France*
[6] *Instituto de Astrofísica, Pontificia Universidad Católica de Chile, Av. Vicuña Mackenna 4860, 7820436 Macul, Santiago, Chile*
[7] *Las Campanas Observatory, Carnegie Institution of Washington, Casilla 601, La Serena, Chile*
[8] *Núcleo de Astronomía de la Facultad de Ingeniería y Ciencias, Universidad Diego Portales, Av. Ejército Libertador 441, Santiago, Chile*
[9] *Tsung-Dao Lee Institute, Shanghai Jiao Tong University, Shanghai 200240, China*
[10] *Department of Astronomy, University of Michigan, 1085 South University Avenue, Ann Arbor, MI 48109, USA*

arXiv:2209.14134v1 [astro-ph.GA] 28 Sep 2022

29 September 2022

ABSTRACT

We use spatially-resolved spectroscopy of a distant giant gravitational arc to test orientation effects on Mg II absorption equivalent width (EW) and covering fraction ($\langle\kappa\rangle$) in the circumgalactic medium of a foreground star-forming galaxy (G1) at $z \sim 0.77$. Forty-two spatially-binned arc positions uniformly sample impact parameters (D) to G1 between 10 and 30 kpc and azimuthal angles α between 30° and 90° (minor axis). We find an EW-D anti-correlation, akin to that observed statistically in quasar absorber studies, and an apparent correlation of both EW and $\langle\kappa\rangle$ with α, revealing a non-isotropic gas distribution. In line with our previous results on Mg II kinematics suggesting the presence of outflows in G1, at minimum a simple 3-D static double-cone model (to represent the trace of bipolar outflows) is required to recreate the EW spatial distribution. The D and α values probed by the arc cannot confirm the presence of a disc, but the data highly disfavor a disc alone. Our results support the interpretation that the EW-α correlation observed statistically using other extant probes is partly shaped by bipolar metal-rich winds.

Key words: galaxies: evolution — galaxies: formation — galaxies: intergalactic medium — galaxies: clusters: individual (SGAS J1226+2152)

1 INTRODUCTION

The galactic-scale kinematics and spatial structure of the high-redshift circum-galactic medium (CGM; Tumlinson et al. 2017; Péroux & Howk 2020, and references therein) is an open topic in our understanding of the baryon cycle of galaxies throughout cosmic time. The cool ($T \sim 10^4$ K) CGM is predicted to have an azimuthal dependence due to the orientation of the material with respect to the central galaxy: galactic outflow signatures are expected to be more prominent along the galaxy's minor axis, while accretion and signatures of extended co-rotating discs may be more readily observable along the major axis (Stewart et al. 2013; DeFelippis et al. 2020; Mitchell et al. 2020; Nelson et al. 2020; Fielding & Bryan 2022). Observationally, such predictions have been addressed statistically using Mg II quasar (e.g., Bouché et al. 2012; Kacprzak et al. 2012; Lan & Mo 2018; Martin et al. 2019) and galaxy (e.g., Bordoloi et al. 2011; Rubin et al. 2018) absorption systems.

On the other hand, spatially resolving the CGM of *individual* galaxies is harder due to the paucity of bright background sources. Mg II in emission has been detected around star-forming galaxies (Burchett et al. 2021; Zabl et al. 2021; Shaban et al. 2021; Leclercq et al. 2022; Rupke et al. 2019), but only in the inner CGM, owing to the emission measure being proportional to density squared.

⋆ E-mail: slopez@das.uchile.cl

© 0000 The Authors

The only opportunity to resolve the extended, diffuse cool CGM is through lensed quasars (e.g., Rauch et al. 2001; Lopez et al. 2007; Zahedy et al. 2016), via projected quasars/galaxies (Péroux et al. 2018; Zabl et al. 2020) or, more recently, using giant gravitational arcs (hereafter "arc-tomography"; Lopez et al. 2018, 2020; Mortensen et al. 2021; Tejos et al. 2021; Bordoloi et al. 2022). In particular, arc-tomography maximizes the number of spatially independent probes per halo and provides an excellent match to CGM scales of up to ~ 100 kpc.

Tejos et al. (2021, hereafter "Paper I") presented arc-tomography data of an isolated star-forming galaxy at $z = 0.77$ towards SGAS J1226+2152, called G1, and focused on its CGM kinematics. Paper I showed that Mg II absorption velocities comply with an extended rotating disc (hereafter ERD; see their Figure 5), implying that part of the cool gas is co-rotating with the inner ionized interstellar gas, similar to what some quasar absorber studies have suggested (Charlton & Churchill 1998; Steidel et al. 2002; Chen et al. 2014; Ho et al. 2017; Rahmani et al. 2018; Zabl et al. 2019). Besides rotation, it presented evidence of out-flowing material from blue-shifted (with respect to systemic) velocity components towards the arc and on top of G1 itself.

In this work we follow up on Paper I to test orientation effects on Mg II absorption equivalent width (EW) around G1. In the first part, based solely on observed quantities, we show that the EW spatial distribution is non-isotropic. In the second part, inspired by Paper I results, we use a 3D toy model for the spatial distribution of EW and find that both a disc and a double cone (that mimics a galactic wind) are required to fit the EW data.

2 DATA

The data used in this work were presented in Paper I, and details on the observations, data reduction, data analysis, and the properties of G1 are provided therein. A brief summary is given below.

The giant arc SGAS J1226+2152 (Koester et al. 2010) is produced by (at least) one $z = 2.9233$ galaxy, lensed by a massive cluster at $z = 0.43$. We observed this field between April 2018 and January 2019 using the Multi-Unit Spectroscopic Explorer (MUSE; Bacon et al. 2010) at the Very Large Telescope. The observations were carried out in Wide-Field mode with Adaptive Optics. The data reduction was performed using the MUSE pipeline (Weilbacher et al. 2012) and residual sky contamination was removed using the Zurich Atmosphere Purge code (Soto et al. 2016). The total integration time of the reduced datacube is 3.6 hours, and the effective PSF FWHM is 0.7″ in the V-band.

The gravitational-arc spectra were optimally averaged leading to binned spaxels of $0.8'' \times 0.8''$ in size in order to (a) increase the signal-noise ratio (S/N) and (b) minimize seeing-induced cross talk between spaxels. In the following, these binned spaxels will be referred to as "positions". SGAS J1226+2152 provides background light to detect Mg II at $z = 0.77138$ in 42 such positions, out of which 27 resulted in significant Mg II detections and 15 non-detections (at 2-σ confidence). A map of Mg II spectra is shown in Figure 3 of Tejos et al. (2021).

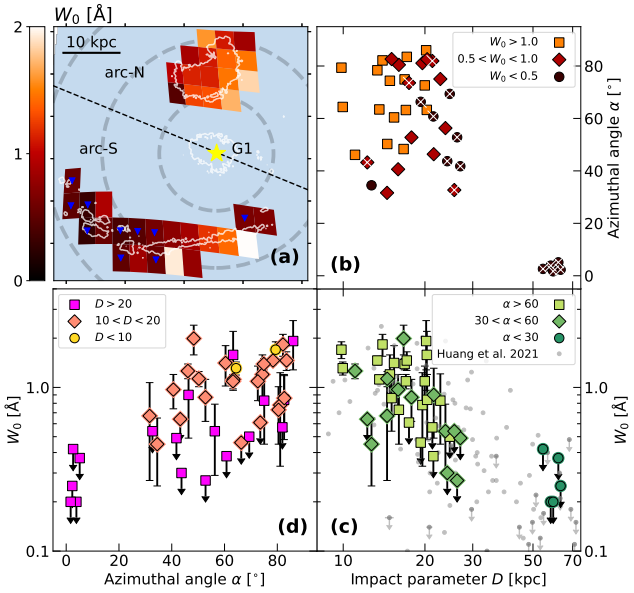


Figure 1. MUSE data of SGAS J1226+2152 with G1 at $z = 0.77138$. Panel (a): rest-frame equivalent-width map around G1 (whose position is marked by a yellow star) obtained from 4×4 binned spaxels and shown here in the de-lensed absorber plane. Blue arrows indicate 2-σ upper bounds. The dashed straight line indicates G1's major axis (Paper I), which we use here to define the azimuthal angle, α. The concentric circumferences mark impact parameters $D = 10$, 20, and 30 kpc. Panels (b)-(c)-(d): the three possible 2-D projections of the (W_0, D, α)-space, color-coded by the remaining parameter according to cuts indicated in the panel labels. The five positions at $D \approx$ 50-70 kpc and $\alpha \approx 0$ (all non-detections) correspond to arc-E (not displayed in Panel (a)). In panel (b) non-detections are indicated with white crosses. In panel (c) grey symbols indicate quasar absorber measurements (Huang et al. 2021) with impact parameters normalized to G1's halo radius.

3 MODEL-INDEPENDENT RESULTS

A map of Mg II λ2796 rest-frame EW (W_0) is displayed in Fig. 1 (a). Each position in the reconstructed ("de-lensed") absorber plane defines an impact parameter, D, and an azimuthal angle, α. D is defined as the projected distance between spaxel centers and G1's light-weighted barycenter; α is the angle between G1's major axis and a line connecting G1 and the spaxel centers, with $\alpha = 0°$ and $\alpha = 90°$ corresponding to the major and minor axes, respectively.

G1's position and inclination angles (PA $= 68°$ and $i = 48°$, respectively) are adopted from the ERD model introduced in Paper I, from which further properties of G1 are: star-formation rate of $1.0 \pm 0.2\,\mathrm{M}_\odot\,\mathrm{yr}^{-1}$, and halo mass of $10^{11.7\pm0.2}\ \mathrm{M}_\odot$.

SGAS J1226+2152 consists of three bright arcs, named arc-N, arc-S, and arc-E (only the first two are shown in Fig. 1 (a); for arc-E, see Paper I). As seen in panels (b), (c), and (d) of Fig. 1, these arcs probe G1's CGM at α uniformly sampled between $\approx 30°$ and $\approx 90°$ at rather similar impact parameters $D \approx$ 10–30 kpc. Compared with previous arc-tomography data, this configuration has an edge to test outflow scenarios along the minor axis, although unfortunately G1 inclination angle is rather low.

Table 1. Mg II statistical properties towards SGAS J1226+2152

(1)	(2)	(3)	(4)	
D	$\langle W_0 \rangle, \sigma_W$	$r_{\alpha W}, p$	$\langle \kappa \rangle$	
kpc	Å		$\alpha > 45°$	$\alpha < 45°$
0–20	$(1.13, 0.38)^a$	$(0.33, 0.15)^a$	$0.90^{+0.05}_{-0.09}$	$0.75^{+0.15}_{-0.25}$
20–30	$(0.87, 0.48)^a$	$(0.43, 0.40)^a$	$0.60^{+0.14}_{-0.16}$	$0.00^{+0.25}_{-0.00}$

(1) Impact parameter; (2) EW median and standard deviation; (3) EW vs. α Pearson correlation coefficient and corresponding two-tailed p-value;(4) Covering fraction for $W_0 > 0.3$ Å and 1-σ errors.
[a] Detections only.

3.1 Impact parameter dependence

Fig. 1 (c) shows W_0 versus D. The usual anti-correlation seen in quasar absorbers (e.g., Chen et al. 2010; Nielsen et al. 2013; Huang et al. 2021) is observed, but thanks to our arc-tomography technique we see it here around an *individual* galaxy at intermediate redshift. Having this spatial information reduces biases introduced from heterogeneous halo masses and mis-assignments in galaxy-QSO pair samples (e.g., Ho et al. 2020, and references therein).

For comparison, quasar absorbers (Huang et al. 2021, grey symbols) are displayed, with impact parameters normalized to G1 halo radius (123 kpc; Paper I). The EW scatter in the quasar sample (0.46 and 0.49 Å at $0 < D < 20$ kpc and $20 < D < 30$ kpc, respectively) is comparable with the scatter around G1 (Table 1). This differs from previous arc-tomography results (Lopez et al. 2018, 2020), where the EW scatter is significantly lower than in quasar absorbers. An assessment of this difference, though, is beyond the scope of this paper.

3.2 Azimuthal angle dependence

Panel (d) of Fig. 1 shows W_0 versus α. Splitting into ranges of D, a mild trend is detected of stronger systems aligned with the minor axis in both D ranges using a Pearson correlation test (Null-hypothesis rejected at just $\approx$ 1-σ confidence; Table 1). However, this correlation may be affected, if not driven, by the $W_0 - D$ anti-correlation combined with the particular arc orientation with respect to the galaxy.

While not included in the statistical test, this potential W_0-α correlation is supported by the lack of detections along the major axis (discussed in § 3.3) combined with strong absorption along the minor axis. Indeed, there is a clear paucity of weak systems ($W_0 < 0.5$ Å) along the minor axis ($\alpha \gtrsim 70°$), suggesting some geometrical effect. We note most of these measurements come from spaxels along the West-side of arc-N, where the S/N is highest. We conclude that there is likely an azimuthal dependence on the measured EW across the arc, although our statistical tests are indecisive.

An azimuthal effect around G1 would be consistent with Mg II averages around star-forming galaxies at similar impact parameters ($D < 40$ kpc), using stacked spectra of either quasars (Lan & Mo 2018) or galaxies (Bordoloi et al. 2011). Unfortunately, due to the lack of spaxels with $\alpha < 30°$ in this range of D, we cannot test claims that Mg II EW is bimodal in α (Bouché et al. 2012; Kacprzak et al. 2012; Martin et al. 2019).

3.3 Anisotropy and covering fraction

Fig. 1 (a) suggests that spaxels towards arc-S have not only lower W_0 values in general but also a higher fraction of non-detections than spaxels towards arc-N. In the $10 < D < 20$ kpc ring, for instance, this cannot be due to different S/N levels, given the stringent (2-σ) upper limits on arc-S. Furthermore, arc-S detections are concentrated along the minor axis. Overall, these trends imply an anisotropic distribution of the enriched cold gas around G1 at distances $\approx 1/5$ of the virial radius.

Thanks to arc-tomography, we can assess this effect quantitatively through the Mg II gas covering fraction, $\langle \kappa \rangle$, obtained from a binomial distribution of detections and non-detections (Chen et al. 2010). Table 1 displays $\langle \kappa \rangle$ using a $W_0 > 0.3$ Å cutoff in two bins of D and α. The bins in D exclude the 5 large D (and low α) arc-E non-detections. The bins in α are arbitrarily split at 45°, which, although resulting in samples of different sizes (6 "major-axis" spaxels and 29 "minor-axis" spaxels), removes the selection function introduced by the particular arc/absorber geometry. $\langle \kappa \rangle$ appears larger towards the minor axis in both low and high impact parameter bins ($\approx$ 1-σ and 3-σ significance, respectively).

Combining all the spaxels (i.e., $D < 30$ kpc), $\langle \kappa \rangle = 0.80^{+0.06}_{-0.08}$ (for $\alpha > 45°$) and $0.43^{+0.18}_{-0.17}$ ($\alpha < 45°$). These figures suggest that directions closer to the minor axis have higher covering fraction than those at $\approx 30°$ from the major-axis, supporting more clumpiness along the latter, i.e., suppresion of Mg II on kpc scales.

This minor axis $\langle \kappa \rangle$ is coincident with quasar absorber values (Kacprzak et al. 2012; Huang et al. 2021) (for $D < 40$ kpc and same W_0 cutoff) around isolated star-forming galaxies. On the other hand, a $\langle \kappa \rangle$-α *correlation* like the one found here is not significantly seen in the Huang et al. (2021) sample, or is simply different than that in the Kacprzak et al. (2012) sample (where $\langle \kappa \rangle$ peaks both at high *and* low α). While we could elaborate on how sample selection affects these apparent mismatches, we caution that due to individual spaxels having a spatial extent our measurements are intrinsically different from $\langle \kappa \rangle$ measured towards point-source quasars; thus, both measurements are not directly comparable, at least using the same W_0 cutoff.

4 TOY MODEL OF THE GAS DISTRIBUTION

To help interpret the present (W_0, D, α) data, and inspired by Paper I ERD model, we attempt a 3-D toy model for the spatial distribution *of EW only*, i.e., we do not include the effects of kinematics or clumpiness.

4.1 Model parameters and MCMC simulations

Our model consists of a main (static) disc and a double cone that mimics the possible trace of a biconical wind (Shopbell & Bland-Hawthorn 1998; Heckman et al. 2000; Ohyama et al. 2002; Bouché et al. 2012; Schroetter et al. 2019). Both produce a smooth EW distribution on the plane of the sky.

A schematic of the model is found in Fig. 2. The main disc is an inclined, infinitely thin disc at the position of G1. PA and inclination are adopted from Paper I ERD model.

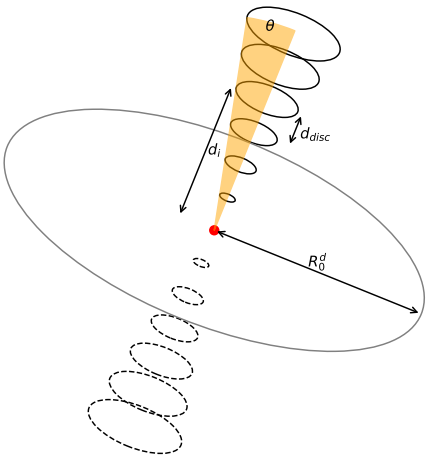


Figure 2. Model schematic

Table 2. MCMC parameter priors

Parameter	Min. Value	Max. Value
W_0^d [Å]	0.0	5.0
R_0^d [kpc]	0.0	100.0
θ [°]	0.0	90.0
W_0^c [Å]	0.0	0.2

On the main disc EW is a function of distance to its center (R) only: $W_0 = W_0^d \exp(-R/R_0^d)$, where W_0^d and R_0^d are maximum EW and characteristic radius, respectively.

The double cone is implemented by stacking $n_{\rm disc}$ parallel and concentric discs on either side of the main-disc along its axis of symmetry. These discs have radii $d_i \tan\theta$, where θ is the half opening angle of a cone and d_i the distance of the i-th disc to the center of G1 along the axis of symmetry. The discs are separated by a constant distance $d_{\rm disc}$ from each other. For ease of implementation, each "truncated" disc contributes with a constant EW, i.e., $W_0 = W_0^c$.

The total synthetic EW is the sum of both contributions along the line-of-sight and is evaluated at a given RA-DEC coordinate.

We perform Monte Carlo Markov Chain (MCMC) simulations on the (RA-DEC,EW) data in order to (a) find representative parameters for comparing models and (b) study degeneracies in the model given our data. The following four model parameters are considered W_0^d, R_0^d, θ and W_0^c. For these four parameters we assume uniform priors between the minimum and maximum values listed in Table 2. For the disc-only model the cone model parameters are fixed to 0, and vice versa for the cone-only model. The rest of the model parameters are fixed at $n_{\rm disc} = 25$ and $d_{\rm disc} = 1$ kpc, i.e., cones extend out to 25 kpc North and South of G1 ($n_{\rm disc}$ and $d_{\rm disc}$ values are less sensible provided their product is constant). The assumed likelihood function ($\mathcal{L}$) for spaxels with detected absorption is given by:

$$\log\mathcal{L} = \sum_i \frac{-(W_{0,i} - W_{model,i}(D_i,\alpha_i))^2}{2\sigma_i^2} - 0.5log(2\pi\sigma_i^2) + n_{con}log(0.954) + n_{incon}log(0.046), \quad (1)$$

where $W_{0,i}$ and σ_i are the detected rest-frame equivalent widths and errors for a given spaxel, and $W_{model,i}(D_i, \alpha_i)$ is the proposed modelled rest-frame equivalent width at the position of the observed spaxel. To account for spaxels with 2σ EW upper limits in the likelihood, we include the probability each spaxel is consistent (95.4 per cent) or inconsistent (4.6 per cent) with the proposed model in the likelihood function to represent the 2σ confidence in the limits. Thus in Equation 1, n_{con} and n_{incon} represent the total number spaxels with EW upper limits that are consistent and inconsistent (respectively) with the proposed model.

Table 3. MCMC results

(1)	(2) W_0^d [Å]	(3) R_0^d [kpc]	(4) θ [°]	(5) W_0^c [Å]	(6) BIC
D	$1.60^{+0.64}_{-0.11}$	$69.75^{+21.03}_{-38.62}$	0^b	0^b	77^{+1}_{-1}
C	0^a	0^a	$36.67^{+0.47}_{-0.84}$	$0.09^{+0.00}_{-0.00}$	34^{+1}_{-1}
D+C	$1.84^{+1.13}_{-1.61}$	$20.92^{+11.04}_{-9.17}$	$22.88^{+13.48}_{-1.38}$	$0.07^{+0.01}_{-0.02}$	40^{+4}_{-2}

(1) Model (D: disc-only; C: cones-only; D+C: disc+cones);
(2) maximum EW on disc; (3) disc's characteristic radius;
(4) Half opening angle; (5) constant EW on cone discs;
(6) Median Bayesian information criterion with ±25-percentile errors.
[a,b]Parameter fixed to 0 to exclude disc or cone component.

4.2 Results and discussion

Setting the appropriate parameters to zero, the model enables 3 flavors: "disc-only", "cones-only", and "disc+cones". For each flavour of model, Table 3 displays the median parameter values from the MCMC with 68% confidence limits along with the median and interquarile range of the Bayesian information criterion. We use these results to compare the different model flavors qualitatively and generate the synthetic EW maps and projections shown in Figure 3 (left-hand column). The corner plots for each of the three model types are provided in the right-hand column of the figure.

For the disc-only model, there appears to be two preferred parameter sets in the respective corner plots (top right of Figure 3), and an apparent degeneracy between W_0^d and R_0^d. More constraints along the major axis would be needed to break the degeneracy. The cones-only model parameter space is well constrained by the data (middle right panel of Figure 3). When comparing to the single component models to the disc+cone model (bottom right of Figure 3), we note that the median value of the disc R_0^d decreases significantly to reduce the EW contribution from the disc component. However, there are two preferred parameter sets. One set is identical to the cone-only model with no disc contribution, while the other set prefers a small disc in addition to cones

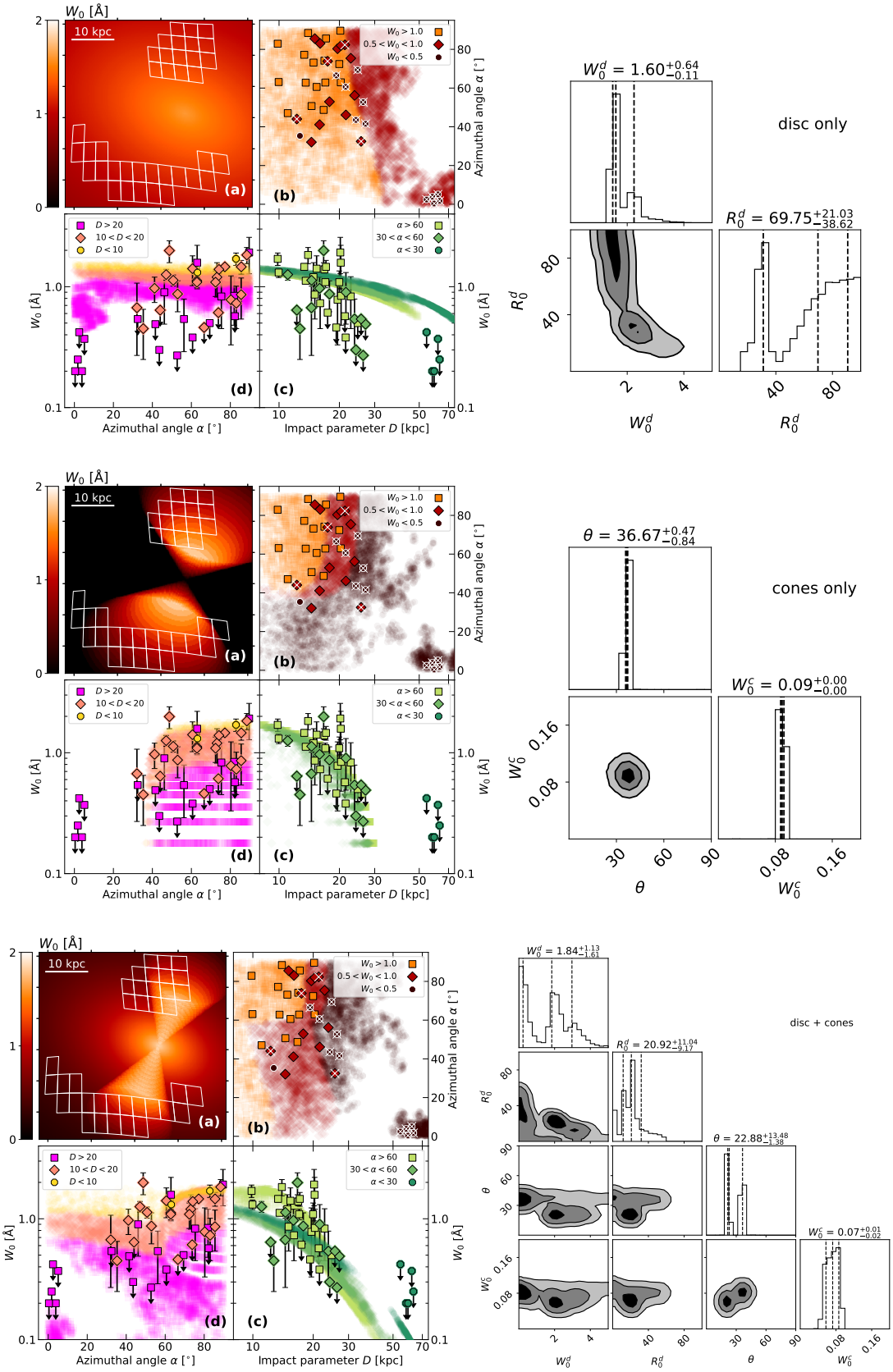


Figure 3. *Left-hand column:* same as Fig. 1 but adding the EW models 'disc-only', 'cones-only', and 'disc+cones' (top to bottom). (a) panels display the synthetic EW maps, with W_0 evaluated in the de-lensed plane at 0.03″ sampling. White rhomboids correspond to the spaxel grid shown in Fig. 1. Panels (b)-(c)-(d) display the three possible 2-D projections of the (W_0, D, α)-space for data and model. Data points have 1-σ error bars and black edges, exactly as in Fig 1. In panel (b) non-detections are indicated with white crosses. The model assumes the median parameter values from the MCMC simulations. W_0, D and α are evaluated at 200 random positions within $\pm$1 kpc of each spaxel center (colored fuzzy points). *Right-hand column:* corresponding corner plots from the MCMC simulations.

with a smaller opening angle ($\theta \approx 23^\circ$). Based on the Bayseian information criterion (Table 3), the data marginally prefers the cones-only model over a disc+cones model. The disc-only model is a poor description of the data.

We warn that, given the lack of data along the major axis, the data are not constraining enough to remove degeneracies in the model parameter space. In particular, the data cannot accurately account for the contribution of the disc at $D \lesssim 30$ kpc in models that include a disc component. Thus we can only use these as toy models. With this disclaimer in mind, a qualitative comparison between data and each model flavor is as follows:

1. *Disc-only model*: The α-D projection (Panel b) is not as well reproduced visually as for models including cones. W_0-D (c) also offers a poor fit to the data, showing almost no α-driven scatter. W_0-α (d) is definitively not well reproduced, at least for $D > 10$ kpc.
2. *Cones-only model*: α-D seems better reproduced, with a tapered vertical gradient in W_0 (panel b). A scatter in EW emerges in the W_0-D projection (c) as a consequence of more anisotropy and an W_0-α (d) correlation is recovered, which matches the data reasonably well.
3. *Disc+cones model*: All three projections are at least as well matched as for the cones-only model. Low-(D, α) measurements are not tied to the disc part of the model, although this might be due to the lack of minor axis measurements at $D < 30$ kpc.

We conclude that, at minimum, a "cone-dominated" component is necessary to provide a better description of the present data than a disc-only model. Requiring a cone component suggests that the observed EW scatter in (W_0-D) is driven by anisotropy.

As demonstrated in Paper I, the kinematic data of our system supports an ERD model. However, the EW data presented in this work suggests a more complex model. This apparent discrepancy is likely a result of how the kinematic information is derived, as the MUSE velocity centroids are likely dominated by the highest column density clouds. If these were preferentially located on the disc mid-plane, which Paper I and our model idealize as a thin disc, both kinematics and EW would match. Conversely, if the dominant clouds are distributed symmetrically off the mid-plane, and still entrained by rotation (i.e., a thick disc), then kinematics would be well fitted but EW not, because the line of sight would miss some of the off-disc clouds. This latter situation is possible if galactic-scale outflows are present (Martin et al. 2012; Rubin et al. 2014) or velocity dispersion is high, the latter of which has been suggested for this galaxy (Paper I; Mortensen et al. 2021).

4.3 Caveats

Evidently, a proper model of the CGM must also consider kinematics (Martin et al. 2019; Afruni et al. 2021) as EW is basically a measure of line-of-sight velocity dispersion. But perhaps even more fundamental, our model neglects the physics of winds. Assuming a biconical outflow made of constant EW discs violates mass conservation, which predicts that gas density $\propto d_i^{-1}$ (e.g., Schroetter et al. 2019).

Regarding observational caveats, background light is assumed to be spatially homogeneous within spaxels, which is most likely incorrect on kpc scales. Instead, we assume the spaxel central value is a representative (light-weighted) average, akin to using background galaxies (e.g., Bordoloi et al. 2011; Diamond-Stanic et al. 2016; Zabl et al. 2020). To test robustness we re-ran the simulations with randomized spaxel positions and verified that results do not change within ± 1 kpc (95% confidence limit) of spaxel centers. Atmospheric effects are neglected as well (although our aggressive spatial binning should counteract them). Finally, D and α values are based on the lens model presented in Paper I.

Summarizing, our toy model highlights the power of having spatially-resolved sampling from arc-tomography data to constrain models of the CGM, but also that CGM models require a lot more complexity.

5 SUMMARY AND CONCLUSIONS

We have analyzed arc-tomography data of SGAS J1226+2152 at $z = 0.77$ to assess possible orientation effects on Mg II rest-frame equivalent width, W_0. The arc configuration is well suited given the uniform sampling of impact parameters D and azimuthal angles α (Fig. 1 b) although major axis positions at $D < 30$ kpc are under-represented. We have discussed the 3 projections of the (W_0, D, α)-space and compared them with QSO absorber statistics and with a simple disc + double cone model for the W_0 spatial distribution. Our conclusions are spelled as follows:

1. From observational data alone:
   (a) W_0 and D anti-correlate. The scatter in W_0 is comparable with quasar-absorber statistics.
   (b) W_0 and α mildly correlate, which is consistent with Bordoloi et al. (2011) and Lan & Mo (2018).
   (c) Covering fraction and α correlate, suggesting less clumpiness along the minor axis.
   (d) 2-D projections of the (W_0, D, α)-space are difficult to control by the remaining parameter. The most deterministic diagnostics to assess orientation effects is the EW spatial distribution itself, on which 3-D models of the CGM can be tested.
2. From a comparison with W_0 by model:
   (a) The data favours a double cone model component, mimicking the trace of a galactic wind.
   (b) Both the α-D and the W_0-α projections are model constraining, specially the former, which reflects the arc/galaxy configuration. W_0-D is the least constraining due to W_0 anisotropy, although it can help to reject some models if α is well sampled.
   (c) α seems to be a key parameter in constraining models of the CGM, that so far can only be done in a less-biased fashion with arc-tomography.

Gravitational arc-tomography provides unprecedented opportunities for assessing the spatial structure of the high-redshift CGM. We look forward to new arc configurations with appropriate D and α samplings, ideally intercepting more inclined galaxies, through which we expect orientation effects to be strongest. Irrespective of this, we hope that the current results will help to better interpret single-sightline

absorber samples.

ACKNOWLEDGMENTS

We thank the anonymous referee for their careful review and comments that improved the quality of this paper. We also warmly thank Eric Jullo for discussions on gravitational lensing. This paper is based on observations collected at the European Southern Observatory under ESO programme(s) 0101.A-0364(A) (PI Lopez). AF, SL, NT, and MH acknowledge support by FONDECYT grant 1191232. EJJ acknowledges support from FONDECYT Iniciación en investigación Project 11200263.

DATA AVAILABILITY

The data may be accessed from the ESO Archive at `http://archive.eso.org/` using the above program ID.

REFERENCES

Afruni A., Fraternali F., Pezzulli G., 2021, MNRAS, 501, 5575
Bacon R., et al., 2010, in Ground-based and Airborne Instrumentation for Astronomy III. p. 773508, doi:10.1117/12.856027
Bordoloi R., et al., 2011, ApJ, 743, 10
Bordoloi R., et al., 2022, Nature, 606, 59
Bouché N., Hohensee W., Vargas R., Kacprzak G. G., Martin C. L., Cooke J., Churchill C. W., 2012, MNRAS, 426, 801
Burchett J. N., Rubin K. H. R., Prochaska J. X., Coil A. L., Vaught R. R., Hennawi J. F., 2021, ApJ, 909, 151
Charlton J. C., Churchill C. W., 1998, ApJ, 499, 181
Chen H.-W., Helsby J. E., Gauthier J.-R., Shectman S. A., Thompson I. B., Tinker J. L., 2010, ApJ, 714, 1521
Chen H.-W., Gauthier J.-R., Sharon K., Johnson S. D., Nair P., Liang C. J., 2014, MNRAS, 438, 1435
DeFelippis D., Genel S., Bryan G. L., Nelson D., Pillepich A., Hernquist L., 2020, ApJ, 895, 17
Diamond-Stanic A. M., Coil A. L., Moustakas J., Tremonti C. A., Sell P. H., Mendez A. J., Hickox R. C., Rudnick G. H., 2016, ApJ, 824, 24
Fielding D. B., Bryan G. L., 2022, ApJ, 924, 82
Heckman T. M., Lehnert M. D., Strickland D. K., Armus L., 2000, ApJS, 129, 493
Ho S. H., Martin C. L., Kacprzak G. G., Churchill C. W., 2017, ApJ, 835, 267
Ho S. H., Martin C. L., Schaye J., 2020, ApJ, 904, 76
Huang Y.-H., Chen H.-W., Shectman S. A., Johnson S. D., Zahedy F. S., Helsby J. E., Gauthier J.-R., Thompson I. B., 2021, MNRAS, 502, 4743
Kacprzak G. G., Churchill C. W., Nielsen N. M., 2012, ApJ, 760, L7
Koester B. P., Gladders M. D., Hennawi J. F., Sharon K., Wuyts E., Rigby J. R., Bayliss M. B., Dahle H., 2010, ApJ, 723, L73
Lan T.-W., Mo H., 2018, ApJ, 866, 36
Leclercq F., et al., 2022, A&A, 663, A11
Lopez S., Ellison S., D'Odorico S., Kim T.-S., 2007, A&A, 469, 61
Lopez S., et al., 2018, Nature, 554, 493
Lopez S., et al., 2020, MNRAS, 491, 4442
Martin C. L., Shapley A. E., Coil A. L., Kornei K. A., Bundy K., Weiner B. J., Noeske K. G., Schiminovich D., 2012, ApJ, 760, 127
Martin C. L., Ho S. H., Kacprzak G. G., Churchill C. W., 2019, ApJ, 878, 84
Mitchell P. D., Schaye J., Bower R. G., 2020, MNRAS, 497, 4495
Mortensen K., Keerthi Vasan G. C., Jones T., Faucher-Giguère C.-A., Sanders R. L., Ellis R. S., Leethochawalit N., Stark D. P., 2021, ApJ, 914, 92
Nelson D., et al., 2020, MNRAS, 498, 2391
Nielsen N. M., Churchill C. W., Kacprzak G. G., 2013, ApJ, 776, 115
Ohyama Y., et al., 2002, PASJ, 54, 891
Péroux C., Howk J. C., 2020, ARA&A, 58, 363
Péroux C., Rahmani H., Arrigoni Battaia F., Augustin R., 2018, MNRAS, 479, L50
Rahmani H., et al., 2018, MNRAS, 474, 254
Rauch M., Sargent W. L. W., Barlow T. A., Carswell R. F., 2001, ApJ, 562, 76
Rubin K. H. R., Prochaska J. X., Koo D. C., Phillips A. C., Martin C. L., Winstrom L. O., 2014, ApJ, 794, 156
Rubin K. H. R., Diamond-Stanic A. M., Coil A. L., Crighton N. H. M., Moustakas J., 2018, ApJ, 853, 95
Rupke D. S. N., et al., 2019, Nature, 574, 643
Schroetter I., et al., 2019, MNRAS, 490, 4368
Shaban A., et al., 2021, arXiv e-prints, p. arXiv:2109.13264
Shopbell P. L., Bland-Hawthorn J., 1998, ApJ, 493, 129
Soto K. T., Lilly S. J., Bacon R., Richard J., Conseil S., 2016, MNRAS, 458, 3210
Steidel C. C., Kollmeier J. A., Shapley A. E., Churchill C. W., Dickinson M., Pettini M., 2002, ApJ, 570, 526
Stewart K. R., Brooks A. M., Bullock J. S., Maller A. H., Diemand J., Wadsley J., Moustakas L. A., 2013, ApJ, 769, 74
Tejos N., et al., 2021, MNRAS, 507, 663
Tumlinson J., Peeples M. S., Werk J. K., 2017, ARA&A, 55, 389
Weilbacher P. M., Streicher O., Urrutia T., Jarno A., Pécontal-Rousset A., Bacon R., Böhm P., 2012, in Radziwill N. M., Chiozzi G., eds, Society of Photo-Optical Instrumentation Engineers (SPIE) Conference Series Vol. 8451, Software and Cyberinfrastructure for Astronomy II. p. 84510B, doi:10.1117/12.925114
Zabl J., et al., 2019, MNRAS, 485, 1961
Zabl J., et al., 2020, MNRAS, 492, 4576
Zabl J., et al., 2021, MNRAS, 507, 4294
Zahedy F. S., Chen H.-W., Rauch M., Wilson M. L., Zabludoff A., 2016, MNRAS, 458, 2423